MEDDOCS
Open Access Publisher

ISSN: 2578-8760

Journal of Nanomedicine

Open Access | Research Article

Chitosan-Based Delivery of an Isolated Plant-Derived Bioactive Compound Attenuates Proliferative Signaling Via the RAS–PI3K–AKT–mTOR Axis in Colorectal Cancer

Cletus Anes Ukwubile[1]*; Babagana Modu[2]; Hassan Braimah Yesufu[3]; Sumaila Mejida[4]; Emmanuel Oise Ikpefan[5]

[1]Department of Pharmacognosy, Faculty of Pharmacy, University of Maiduguri, Maiduguri, Nigeria.

[2]Department of Biochemistry, Faculty of Life Sciences, University of Maiduguri, Maiduguri, Nigeria.

[3]Department of Pharmaceutical Chemistry, Faculty of Pharmacy, University of Maiduguri, Maiduguri, Nigeria.

[4]Central Research Laboratory, University of Lagos, Akoka, Lagos, Nigeria.

[5]Department of Pharmacognosy and Traditional Medicine, Faculty of Pharmacy, Delta State University, Abraka, Nigeria.

***Corresponding Author(s): Cletus Anes Ukwubile**

Department of Pharmacognosy, Faculty of Pharmacy, University of Maiduguri, Maiduguri, Nigeria.

Email: doccletus@yahoo.com; caukwubile@unimaid.du.ng

Received: May 11, 2026

Accepted: July 01, 2026

Published Online: July 08, 2026

Journal: Journal of Nanomedicine

Publisher: MedDocs Publishers LLC

Online edition: http://meddocsonline.org/

Keywords: Chitosan nanoparticles; Colorectal cancer; Phytomedicine; RAS signaling; PI3K–AKT–mTOR pathway.

Abstract

Quercetin is a plant-derived flavonoid with established anticancer activity; however, its use is limited by rapid systemic clearance, poor aqueous solubility, and low bioavailability. Nanocarrier-based delivery systems offer a promising strategy to overcome these limitations. This study developed and evaluated Quercetin-Loaded Chitosan Nanoparticles (Q-CS NPs) as an oral phytomedicine-based nanotherapeutic for colorectal cancer. Quercetin was isolated and structurally confirmed using UV–Vis, FTIR, LC-MS, and NMR analyses. The synthesized nanoparticles were physicochemically characterized for particle size, polydispersity, zeta potential, morphology, encapsulation efficiency, drug loading, release kinetics, and thermal stability. In vitro anticancer activity was assessed in HCT116 and HT-29 colorectal cancer cells, with NCM460 normal colon cells as controls. Cytotoxicity, apoptosis induction, and cell-cycle distribution were evaluated, while mechanistic studies examined modulation of the RAS–PI3K–AKT–mTOR signaling pathway using western blotting and immunohistochemistry. In vivo efficacy, biodistribution, and systemic toxicity were investigated in an HCT116 xenograft mouse model following oral administration. Q-CS NPs exhibited nanoscale size, low polydispersity, positive surface charge, high encapsulation efficiency, and sustained drug release. Compared with free quercetin, nanoformulated quercetin reduced cancer cell viability, enhanced apoptosis, and induced cell-cycle arrest. Treatment suppressed tumor growth without weight loss or organ toxicity and enhanced tumor accumulation.

Cite this article: Ukwubile CA, Modu B, Yesufu HB, Mejida S, Ikpefan EO. Chitosan-Based Delivery of an Isolated Plant-Derived Bioactive Compound Attenuates Proliferative Signaling Via The RAS–PI3K–AKT–mTOR Axis in Colorectal Cancer. J Nanomed. 2026; 9(1): 1076. J Nanomed. 2026; 9(1): 1076.

Introduction

Despite advancements in screening, diagnosis, and treatment approaches, Colorectal Cancer (CRC) is one of the most common cancers diagnosed globally and continues to be a major cause of cancer-related mortality, contributing significantly to the global disease burden [1-3]. Due to aggressive tumor biology, metastatic dissemination, and the development of resistance to traditional chemotherapeutic drugs, advanced and metastatic CRC continues to have a dismal prognosis, although early-stage CRC is frequently efficiently controlled [4]. Cumulative genetic and epigenetic changes that converge on carcinogenic signaling pathways controlling cell proliferation, survival, metabolism, and apoptosis are the molecular drivers of colorectal carcinogenesis.

The RAS–Phosphoinositide 3-Kinase (PI3K)–Protein Kinase B (AKT)–Mechanistic Target of Rapamycin (mTOR) signaling axis is one of these pathways that is crucial to the development and progression of colorectal cancer. About 40–50% of colorectal tumors have activating mutations in RAS family genes, especially KRAS, which are significantly linked to the aggressiveness of the illness, a poor prognosis, and resistance to targeted therapy [5]. Tumor growth and treatment resistance are facilitated by aberrant activation of downstream PI3K–AKT–mTOR signaling, which also promotes persistent proliferative signaling, suppression of apoptosis, increased angiogenesis, and metabolic reprogramming [6,7]. For the therapy of colorectal cancer, attenuation of the RAS–PI3K–AKT–mTOR axis is therefore a therapeutically relevant and appealing approach.

Because of their structural diversity and ability to simultaneously affect several molecular targets, bioactive chemicals originating from plants have long been acknowledged as valuable sources of anticancer medicines. A naturally occurring flavonoid found in many fruits, vegetables, and medicinal plants, quercetin has garnered significant interest because of its wide range of pharmacological characteristics, which include anti-inflammatory, antioxidant, and anticancer effects [8,9]. A growing body of research suggests that quercetin suppresses oncogenic signaling pathways, induces apoptosis, and causes cell-cycle arrest to have antiproliferative effects on a variety of cancer types [10]. Quercetin's potential as a multi-targeted therapeutic agent for the treatment of colorectal cancer is highlighted by reports that it modulates important elements of the RAS–PI3K–AKT–mTOR pathway [11-13].

Unfavorable pharmacokinetic characteristics continue to restrict quercetin's clinical translation despite its encouraging anticancer potential. Quercetin's low oral bioavailability, chemical instability, quick systemic elimination, and poor water solubility all limit its effective concentration at tumor sites and reduce its therapeutic efficacy *in vivo* [14,15]. These restrictions highlight the need for novel drug delivery techniques that can improve the stability, bioavailability, and intracellular accumulation of quercetin.

Drug delivery systems based on nanotechnology have become effective instruments to address the pharmacokinetic issues related to phytochemicals. Chitosan, a biodegradable, biocompatible, and cationic polysaccharide produced from chitin, has attracted a lot of attention among different nanocarriers for cancer medication delivery applications [16-18]. Mucoadhesiveness and a positive surface charge are two advantageous physicochemical characteristics of chitosan nanoparticles that enable improved cellular absorption and interaction with negatively charged cancer cell membranes. Additionally, chitosan-based nanocarriers improve bioavailability and therapeutic performance by preventing premature degradation of encapsulated compounds and enabling controlled and sustained drug release [18].

It has been demonstrated that encasing quercetin in chitosan nanoparticles improves its solubility, stability, and intracellular transport, greatly increasing its anticancer activity [16]. In a number of cancer models, quercetin's antiproliferative and pro-apoptotic actions have been shown to be enhanced by chitosan-mediated nanoformulation. Nevertheless, there are still few thorough mechanistic studies that clarify how chitosan-loaded quercetin affects the RAS–PI3K–AKT–mTOR signaling axis in colorectal cancer.

In this work, we used colorectal cancer models to examine the anticancer potential and underlying molecular mechanisms of a chitosan-based delivery system encapsulating quercetin. We postulated that by reducing RAS-driven activation of the PI3K–AKT–mTOR signaling cascade, chitosan-mediated nanoencapsulation would improve quercetin's antiproliferative activity. In order to test this idea, we used an integrated experimental method that combined mechanistic investigations utilizing Western blotting and immunohistochemistry with functional tests such as cell viability and flow cytometry-based apoptosis and cell-cycle analysis. Our results encourage the development of chitosan-based phytomedicinal techniques that target oncogenic signaling pathways in colorectal cancer and offer mechanistic insight into nano-enabled quercetin delivery.

Materials and methods

Chemicals, reagents, and apparatus

Quercetin analytical standard (≥98% purity), low-molecular-weight chitosan (degree of deacetylation ≥85%), sodium Tripolyphosphate (TPP), acetic acid, ethanol, methanol, dimethyl sulfoxide (DMSO), MTT reagent, annexin V–FITC/propidium iodide apoptosis detection kit, and protease/phosphatase inhibitor cocktails were obtained from standard commercial suppliers. Primary antibodies against RAS family proteins, PI3K, phosphorylated and total AKT, phosphorylated and total mTOR, and β-actin were purchased from validated manufacturers. Cell culture media, fetal bovine serum, antibiotics, and other routine reagents were of cell culture or analytical grade. Dynamic light scattering measurements were performed using a particle size analyzer. Flow cytometry was conducted using a multi-color flow cytometer. Western blot analysis employed standard electrophoresis and chemiluminescence detection systems. Electron microscopy was used for nanoparticle morphological assessment.

Plant collection, authentication, and preparation

During the rainy season in 2025, fresh leaves of *Lantana camara* L. were gathered from their natural habitat early in the morning during the wet season. A voucher specimen with the number UMM/FPH/VEB/002 was placed in an institutional herbarium for future reference after the plant was verified by taxonomist Dr. C.A. Ukwubile. The collected leaves were air-dried at room temperature in the shade for two weeks to maintain phytochemical integrity after being properly cleaned with distilled water to eliminate dirt. A mechanical grinder was used to grind the dried plant material into a fine powder, which was then weighed and kept in airtight containers until extraction. A hydro-ethanolic (30:70) solvent was used to extract powdered materials while they were continuously stirred for 72 hours at

room temperature. To create a crude extract for additional purification, the extract was filtered, condensed under low pressure using a rotary evaporator, and then dried.

Isolation and purification of quercetin

Chromatographic methods were used to separate quercetin from the crude plant extract. The extract was eluted using increasingly polar solvent systems after being subjected to column chromatography on silica gel. Using the proper mobile phases, thin-layer chromatography was used to monitor the fractions, which were then visible under UV light. Repeated chromatography was used to further purify fractions that showed chromatographic features compatible with quercetin until a single spot appeared on TLC. For later characterization and formulation research, the isolated chemical was dried and kept at -20°C [19,20].

Characterization of the bioactive compound

The isolated compound was characterized using complementary spectroscopic and spectrometric techniques to confirm its identity as quercetin. First, ultraviolet–visible (UV–Vis) spectroscopy was conducted to determine characteristic absorption peaks in the 200–400 nm range, with expected maxima consistent with flavonoid structures. Fourier-Transform Infrared (FTIR) spectroscopy was performed to identify functional groups, including characteristic hydroxyl and carbonyl stretching bands [21,22]. A high-resolution Quadrupole Time-of-Flight (QTOF) instrument operating in negative Electrospray Ionization (ESI−) mode was used to perform Liquid Chromatography–Mass Spectrometry (LC–MS) for mass-based confirmation, scanning from m/z 50–1000. A C18 reverse-phase column with a water–acetonitrile gradient containing 0.1% formic acid was used for the chromatographic separation. As previously reported for quercetin and its derivatives in plant extracts by LC-HRMS studies, the observed molecular ion peak at m/z is compatible with quercetin's theoretical molar mass (~302 Da) and fragmentation pattern, offering molecular-level confirmation of the flavonoid skeleton [22].

For structural clarification, Nuclear Magnetic Resonance (NMR) spectroscopy was employed. Using deuterated Dimethyl Sulfoxide (DMSO-d6) as the solvent at 298 K, 1H and 13C NMR spectra were obtained on an 800 MHz NMR spectrometer. According to established spectral assignments and the known flavonol structure, typical quercetin signals were found in the aromatic region for ^{1}H NMR (δ ~6.2–7.7 ppm) and corresponding carbon resonances in ^{13}C NMR. Quercetin's identification was further confirmed by the existence of downfield phenolic hydroxyl proton signals. The molecular structure and substitution pattern of quercetin were validated by the combination of precise mass data from LC-MS and NMR chemical shifts [23,24].

Preparation of chitosan-loaded quercetin nanoparticles

With a few modest adjustments, the ionic gelation process previously described was used to create chitosan-loaded quercetin nanoparticles [25]. After dissolving 2 mg/mL of chitosan in 1% (v/v) acetic acid, the pH was brought between 4.8 and 5.0. After dissolving quercetin in ethanol, it was gradually added to the chitosan solution while being continuously stirred. At room temperature, TPP solution (1 mg/mL) was gradually added at a mass ratio of 4:1 between chitosan and TPP while being continuously stirred. Chitosan and TPP interacted electrostatically to produce nanoparticles. After 30 more minutes of stirring, the mixture was centrifuged, cleaned to get rid of any unencapsulated quercetin, and lyophilized for subsequent research.

Physicochemical characterization

Particle size measurement

Quercetin-loaded chitosan nanoparticles' physicochemical characteristics were methodically described. Dynamic light scattering (DLS) was used to assess the particle size distribution, Polydispersity Index (PDI), and zeta potential (Zetasizer Nano series, Malvern Instruments). To prevent multiple scattering effects, nanoparticle suspensions were suitably diluted with deionized water before testing. Each measurement was done in triplicate at 25°C, and the mean ± standard deviation was used to express the results [25].

Morphological examination

Electron microscopy was used to analyze the surface properties and morphology of nanoparticles. Particle shape, surface texture, and dispersion homogeneity were evaluated by air-drying and imaging a drop of diluted nanoparticle suspension on a carbon-coated copper grid [26].

Entrapment efficiency

By measuring the amount of unencapsulated quercetin in the supernatant following nanoparticle centrifugation, Encapsulation Efficiency (EE%) and Drug Loading (DL%) were indirectly calculated. Using a previously developed calibration curve, the concentration of free quercetin was determined spectrophotometrically at 370 nm. Based on the total amount of quercetin initially added and the amount that remained unencapsulated, established equations were used to compute encapsulation efficiency and drug loading [25,27].

Fourier-transform infrared (FTIR) spectroscopy

To assess the chemical interactions between quercetin and chitosan and verify effective encapsulation, FTIR spectroscopy was used. Pure quercetin, blank chitosan nanoparticles, and quercetin-loaded nanoparticles all had FTIR spectra that fell between 4000 and 400 cm^{-1}. In order to detect intermolecular interactions like hydrogen bonding, shifts or modifications in distinctive absorption bands were examined [25].

In vitro drug release and drug kinetics

In vitro drug release and release kinetics were evaluated using a dialysis method under physiological conditions. Quercetin-loaded nanoparticles were suspended in phosphate-buffered saline (PBS, pH 7.4) and maintained at 37 °C with constant agitation. At predetermined time intervals, aliquots were withdrawn and replaced with fresh buffer. The amount of released quercetin was quantified spectrophotometrically at 370 nm. Cumulative release data were fitted to kinetic models, including zero-order, first-order, Higuchi, and Korsmeyer–Peppas models, to elucidate the mechanism of quercetin release from the chitosan matrix [16,17,26,28].

Thermal stability analysis

Thermal stability and physicochemical integrity of the nanoparticles were assessed using thermal analysis. Differential Scanning Calorimetry (DSC) was performed to evaluate thermal transitions and possible changes in crystallinity following quercetin encapsulation. Thermogravimetric Analysis (TGA) was conducted to assess thermal degradation patterns and stability by recording weight loss as a function of temperature under controlled heating conditions. Comparative analysis of pure quercetin, blank chitosan nanoparticles, and quercetin-loaded

nanoparticles was used to confirm improved thermal stability following nano-encapsulation [29,30].

Cell culture

In vitro tumor models were created using the human colorectal cancer cell lines HCT116 and HT-29. A normal human colon epithelial cell line (NCM460) was used concurrently to assess the therapies' biocompatibility and selectivity. Before being used, all cell lines were verified and acquired from a reputable cell bank. The cells were kept in Dulbecco's Modified Eagle's Medium (DMEM) supplemented with 100 U/mL penicillin, 100 µg/mL streptomycin, and 10% (v/v) heat-inactivated Fetal Bovine Serum (FBS). Cultures were kept in a humidified environment with 5% CO2 at 37°C. When cells reached about 70–80% confluence, they were subcultured using normal trypsinization techniques after being regularly checked for morphology and confluence. Before being exposed to test formulations for experimental treatments, cells were sown at the proper densities and given an overnight chance to adhere. Free quercetin, blank chitosan nanoparticles, and quercetin-loaded chitosan nanoparticles at specified doses and time intervals were used as treatments. Equivalent quantities of vehicle alone were given to control cells. To guarantee reproducibility, every experiment was conducted in triplicate [31].

Cell viability assay

The MTT assay was used to measure cell viability. Using 100 µL of complete growth media, HCT116, HT-29, and NCM460 cells were seeded into 96-well plates at a density of 5×10^3 cells per well and left to adhere overnight. After attachment, cells were exposed to doses ranging from 5 to 100 µg/mL of free quercetin, blank chitosan nanoparticles, or quercetin-loaded chitosan nanoparticles. The vehicle-only medium was given to the control wells. Following 24, 48, and 72 hours of treatment, each well received 10 µL of MTT solution (5 mg/mL in phosphate-buffered saline), which was then incubated for an extra 4 hours at 37°C. After carefully removing the culture media, the formazan crystals were completely dissolved by shaking them gently in 100 µL of Dimethyl Sulfoxide (DMSO). A microplate reader was used to measure absorbance at 570 nm, with background adjustment at 630 nm. In comparison to untreated control cells, cell viability was expressed as a percentage. Nonlinear regression analysis was used to compute half-maximal inhibitory concentration (IC_{50}) values and create dose-response curves [32-34]. Every experiment was carried out independently at least three times and in triplicate.

Flow cytometry analysis

Using flow cytometry, apoptosis and cell-cycle distribution were examined. In short, 6-well plates were seeded with HCT116 and HT-29 colorectal cancer cells at a density of 2×10^3 cells per well, and the cells were left to adhere overnight. For a duration of 24 hours, cells were exposed to either free quercetin, blank chitosan nanoparticles, or quercetin-loaded chitosan nanoparticles at concentrations that matched their corresponding IC_{50} values. As controls, untreated cells were used. Cells were extracted, twice cleaned with cold Phosphate-Buffered Saline (PBS), and then resuspended in binding buffer for apoptosis investigation. Following the manufacturer's instructions, cells were stained with Propidium Iodide (PI) and annexin V-FITC and allowed to sit at room temperature in the dark for 15 minutes. In order to identify viable, early apoptotic, late apoptotic, and necrotic cell populations, samples were examined right away. Treated and control cells were frozen in 70% ice-cold ethanol and kept at −20°C for a minimum of 12 hours in order to perform cell-cycle analysis. The fixed cells were stained with propidium iodide (50 µg/mL) for 30 minutes at room temperature in the dark after being rinsed with PBS and treated with RNase A (100 µg/mL). The distribution of cells across G0/G1, S, and G2/M phases was ascertained by analyzing DNA content. A BD FACSCantoTM II flow cytometer (BD Biosciences, USA) was used for flow cytometric collection, recording at least 10,000 events per sample. FlowJo software (version 10.8.1; BD Biosciences, USA) was used to analyze the data. Cell-cycle phase distribution and the fraction of apoptotic cells were quantitatively analyzed [34–36]. Every experiment was carried out three times.

Western blot analysis

Protease and phosphatase inhibitor cocktails (Sigma-Aldrich) were added to the radioimmunoprecipitation assay (RIPA) buffer to recover total cellular protein from both treated and control cells. Protein concentrations were measured using a Bicinchoninic Acid (BCA) protein assay kit in accordance with the manufacturer's instructions after cell lysates were cleared by centrifugation at 12,000×g for 15 minutes at 4°C. Sodium Dodecyl Sulfate–Polyacrylamide Gel Electrophoresis (SDS–PAGE) was used to separate equal amounts of protein (30–40 µg per lane), which were then transferred onto Polyvinylidene Difluoride (PVDF) membranes. For one hour at room temperature, membranes were blocked using either 5% non-fat dried milk or 5% bovine serum albumin in Tris-buffered saline with 0.1% Tween-20 (TBST). Membranes were incubated overnight at 4°C with the following primary antibodies: anti-RAS (Cell Signaling Technology, Cat. No. 3339, 1:1000), anti-PI3K p85 (Cell Signaling Technology, Cat. No. 4292, 1:1000), anti-phospho-AKT (Ser473) (Cell Signaling Technology, Cat. No. 4060, 1:1000), anti-total AKT (Cell Signaling Technology, Cat. No. 9272, 1:1000), anti-phospho-mTOR (Ser2448) (Cell Signaling Technology, Cat. No. 5536, 1:1000), anti-total mTOR (Cell Signaling Technology, Cat. No. 2983, 1:1000), and anti-β-actin (Cell Signaling Technology, Cat. No. 4970, 1:5000) [7,35].

To guarantee uniform protein loading and transfer efficiency throughout all samples, β-actin was employed as the internal loading control. Following TBST washing, membranes were incubated for one hour at room temperature with the proper horseradish peroxidase-conjugated secondary antibodies (anti-rabbit IgG, Cell Signaling Technology, Cat. No. 7074, 1:5000). An Enhanced Chemiluminescence (ECL) detection system was used to visualize protein bands, and a chemiluminescence documentation system was used to take pictures. Target protein expression levels were adjusted to β-actin using ImageJ software for densitometric analysis. Every experiment was carried out independently at least three times and in triplicate [37,38].

Immunohistochemistry

Tumor tissue sections that were 4 µm thick and Formalin-Fixed, Paraffin-Embedded (FFPE) were produced for immunohistochemical examination. After being deparaffinized in xylene, sections were rehydrated using a series of graded ethanol solutions. Citrate buffer (10 mM, pH 6.0) and heat-induced epitope retrieval in a pressure cooker were used for antigen retrieval. In order to reduce nonspecific binding, endogenous peroxidase activity was quenched by incubation with 3% hydrogen peroxide and then blocked with normal serum. Primary antibodies that target important elements of the RAS–PI3K–AKT–mTOR signaling cascade, such as RAS, phospho-AKT, and

phospho-mTOR, were added to sections and incubated overnight at 4°C at optimum dilutions. Sections were treated with a horseradish peroxidase-conjugated secondary antibody using an EnVisionTM detection system (Dako, Agilent Technologies) after the primary antibody was incubated. 3,3'-Diaminobenzidine (DAB) was used as the chromogen to visualize immunoreactivity, and hematoxylin was used as a counterstain. A Leica DM2000 LED light microscope (Leica Microsystems, Germany) with a digital camera was used to view and photograph immunostained sections. The percentage of positively stained cells and staining intensity were used to semi-quantitatively rate the staining intensity and distribution in representative tumor locations. To reduce observer bias, all IHC studies were carried out in a blinded fashion [39-41].

Biodistribution analysis

Fluorescence-based imaging was used to assess the quercetin-loaded chitosan nanoparticles' in vivo biodistribution. In order to facilitate non-invasive tracking, nanoparticles were fluorescently labeled using a near-infrared fluorescent probe before being administered. Animals with tumors were randomly randomized to treatment groups and given an intravenous injection of either free fluorescent probe or fluorescently labeled chitosan nanoparticles loaded with quercetin at an equivalent dose. Whole-body imaging was carried out utilizing an *in vivo* imaging system (IVIS Spectrum, PerkinElmer, USA) under isoflurane anesthesia at predefined time intervals following delivery (1, 6, 12, 24, and 48 hours). Standardized excitation and emission filter settings were used to get fluorescence signals, and the distribution and accumulation of nanoparticles in tumors and key organs were evaluated using image analysis [16,42,43].

Major organs, such as the liver, spleen, kidneys, lungs, heart, and tumor tissues, were removed for ex vivo fluorescence imaging after the animals were put to sleep. Living Image software was used to quantify the fluorescence intensity and create Regions of Interest (ROIs) for each organ. In order to compare free and nano-encapsulated formulations, biodistribution was represented as radiant efficiency or fluorescence intensity per unit area. This investigation gave insight into the improved delivery capability of the nanocarrier system by assessing the tumor-targeting effectiveness, systemic dispersion, and preferential accumulation of quercetin-loaded nanoparticles in comparison to free quercetin.

Experimental animals and ethical consideration

For *in vivo* research, male BALB/c nude mice weighing 20–25g and aged 6–8 weeks were utilized. The animals were kept in typical laboratory settings with free access to food and water, a 12-hour light/dark cycle, a temperature of 22±2°C, and a relative humidity of 55±10%. The Institutional Animal Ethics Committee authorized all experimental procedures, which were carried out in compliance with institutional norms for the use and care of laboratory animals.

Tumor xenograft establishment

HCT116 cells were collected during the exponential growth phase, cleaned, and resuspended in sterile phosphate-buffered saline in order to create a colorectal cancer xenograft model. One hundred microliters of viable HCT116 cells were subcutaneously injected into each mouse's right flank. Digital calipers were used to track the growth of the tumor, and the following formula was used to determine the tumor volume [44-46]:

$$V = (\text{length} \times \text{width}^2)/2. \quad (1)$$

Treatment was initiated when tumors reached an average volume of approximately 100–120 mm^3.

Oral treatment protocol

Tumor-bearing mice were randomly allocated into four experimental groups (n = 6 per group):

(i) vehicle control (0.5% carboxymethylcellulose),

(ii) free quercetin (**50 mg/kg body weight**),

(iii) blank chitosan nanoparticles (administered at an equivalent nanoparticle mass), and

(iv) quercetin-loaded chitosan nanoparticles (**equivalent to 50 mg/kg body weight of quercetin**).

Blank chitosan nanoparticles were given at an equivalent nanoparticle mass, whereas free quercetin and quercetin-loaded chitosan nanoparticles were given orally by gavage at an equivalent quercetin dose of 50 mg/kg body weight. For 21 days in a row, each treatment was administered once daily. To guarantee consistent dosage and stability, all formulations were made fresh and suspended in 0.5% Carboxymethylcellulose (CMC). Based on earlier research showing quercetin's safety and antitumor activity after oral administration, as well as the capacity of chitosan nanoparticles to improve gastrointestinal stability and bioavailability, the chosen dosage and oral route were chosen [44].

Evaluation of tumor growth and body weight

Throughout the course of treatment, body weight and tumor dimensions were noted every three days. By comparing the tumor volumes at the conclusion of treatment between groups, tumor growth inhibition was computed. Changes in body weight were tracked as a measure of oral tolerance and systemic toxicity.

Terminal sample collection

Animals were put to death under anesthesia at the conclusion of the treatment period. In order to assess modification of the RAS–PI3K–AKT–mTOR signaling pathway, tumors were removed, weighed, and prepared for subsequent investigations, such as Western blotting and immunohistochemistry. The liver, kidneys, spleen, heart, and lungs were among the major organs that were gathered for histological analysis and toxicity evaluation.

Toxicity evaluation of quercetin-loaded chitosan nanoparticles

To determine the biocompatibility and safety profile of quercetin-loaded chitosan nanoparticles, their systemic toxicity was assessed in vivo. Quercetin-loaded chitosan nanoparticles, free quercetin, blank chitosan nanoparticles, or vehicle control were given to tumor-bearing animals at therapeutically relevant doses via the specified route of administration after they were randomly assigned to treatment and control groups. Over the course of the experiment, treatments were administered in compliance with institutional ethical standards. Every day, the animals' body weight, food consumption, grooming habits, and any indications of toxicity or suffering were tracked. To evaluate the systemic effects of treatment, body weights were measured on a regular basis and compared between groups. Blood samples were taken for hematological and serum biochemical tests after

the animals were put to death at the conclusion of the treatment period. Hepatic and renal function were assessed by measuring important markers such as urea, creatinine levels, aspartate aminotransferase, and alanine aminotransferase [45-47].

For histological analysis, major organs such as the liver, kidneys, heart, lungs, and spleen were removed, fixed in 10% neutral-buffered formalin, embedded in paraffin, sectioned, and stained with hematoxylin and eosin. Under a microscope, tissue sections were inspected for signs of necrosis, cellular deterioration, inflammation, or other pathological changes. To find out if nano-encapsulation reduced systemic negative effects, the toxicity profile of quercetin-loaded chitosan nanoparticles was compared to that of free quercetin and control groups.

Statistical analysis

Data were expressed as mean ± SD (n=3 repetitive readings). The value of $p < 0.05$ or $p < 0.01$ was considered significant using one-way ANOVA followed by Tukey's post hoc test. Statistical analysis was performed using GraphPad Prism version 9.

Results

Isolation and purification of quercetin

Column chromatography on silica gel was used to successfully separate quercetin from the crude plant extract. Thin-Layer Chromatography (TLC) was used to monitor the various fractions that were produced by gradient elution using more polar solvents. For additional purification, fractions having retention factor (R_f) values consistent with standard quercetin ($R_f \approx 0.55$ in chloroform: methanol; 9:1) and a single spot under Ultraviolet (UV) light at 254 and 366 nm were combined (Figure 1A and B). These pooled fractions underwent repeated column chromatography, which confirmed the isolated compound's high purity by producing a single, distinct spot-on TLC. Purified quercetin was obtained as a yellow crystalline powder that was stable at -20 °C. It was then utilized for the creation of nanoparticles and physicochemical characterization. The total yield of purified quercetin from the crude extract was roughly 2.8 ± 0.2% (w/w) (Figure 1C), which is consistent with yields from comparable plant sources that have been reported [3,4]. The isolated compound's potential for additional analytical and biological evaluation was supported by visual inspection and TLC analysis, which showed that it was free of detectable impurities (Figure 1A-C).

Characterization of the bioactive compound

The purified compound was characterized using complementary spectroscopic and spectrometric techniques to confirm its identity as quercetin.

UV–visible spectroscopy: The isolated compound's UV-Vis spectra showed distinctive absorption maxima at 256 and 370 nm (Figure 2A), which are in line with the conjugated π–π* transitions of the A and B rings of flavonols. These maxima show that the flavonoid backbone of quercetin has been preserved, which is consistent with reported values [5,6].

Fourier-transform infrared (FTIR) spectroscopy: FTIR examination showed significant absorption bands at about 3400 cm^{-1} for the O–H stretching of phenolic hydroxyl groups, 1660 cm^{-1} for the C=O stretching of the carbonyl group, and additional peaks at 1600–1450 cm^{-1} for aromatic C=C stretching (Figure 2B). According to the structure of quercetin, the FTIR profile verified the existence of distinctive functional groups of flavonols [7].

Liquid chromatography–mass spectrometry (LC–MS): A quadrupole time-of-flight (QTOF) mass spectrometer operating in negative Electrospray Ionization (ESI−) mode was used for high-resolution LC–MS analysis, scanning from m/z 50–1000 (Figure 2C). A C18 reverse-phase column with a water–acetonitrile gradient containing 0.1% formic acid was used for chromatographic separation. In accordance with the theoretical molar mass of quercetin (~302 Da), the isolated molecule showed a molecular ion peak at m/z 301.03 $[M–H]^-$. The flavonoid skeleton was further supported by fragmentation patterns, such as the typical loss of CO and CO_2 units. Quercetin was definitively confirmed at the molecular level by the precise mass measurement and MS/MS spectra [8,9].

Nuclear magnetic resonance (NMR) spectroscopy: Using ^1H and ^{13}C NMR spectroscopy on an 800 MHz NMR spectrometer with DMSO-d6 as the solvent at 298 K, structural elucidation was carried out. ^1H NMR spectra revealed aromatic proton signals in the δ 6.2–7.7 ppm range, which are consistent with the B-ring and A-ring protons of quercetin. Between δ 9.0 and 12.5 ppm, signals related to downfield phenolic hydroxyl protons were detected (Figure 2D).C NMR spectra showed resonances at δ 93–178 ppm that matched known assignments for quercetin and corresponded to the conjugated C=O carbonyl and aromatic carbons. The substitution pattern and flavonol framework were validated by the combination of ^1H and ^{13}C chemical shifts [10,11].

When combined, these complementary methods—UV-Vis, FTIR, LC-MS, and NMR—confirmed the isolated compound's identification, purity, and structural integrity as quercetin, confirming its appropriateness for further biological research and nanoparticle manufacturing.

Physicochemical characterization

To verify successful formation, stability, and appropriateness for biological applications, the physicochemical characteristics of quercetin-loaded chitosan nanoparticles were thoroughly assessed. Quercetin-loaded chitosan nanoparticles showed a nanoscale particle size distribution with a limited dispersity, indicating homogeneous particle production, according to Dynamic Light Scattering (DLS) studies. The polydispersity index (PDI < 0.3) indicated a homogeneous population of nanoparticles, and the mean hydrodynamic diameter was within the ideal range for cellular uptake. Quercetin was successfully incorporated into the polymeric matrix, as seen by the somewhat lower average size of blank chitosan nanoparticles (Figure 3A).

Zeta potential studies revealed that quercetin-loaded nanoparticles had a positive surface charge, which was caused by chitosan's protonated amino groups. Because of electrostatic repulsion, the positive zeta potential indicated strong colloidal stability and is advantageous for contact with negatively charged cell membranes. The addition of quercetin caused a slight decrease in surface charge in comparison to blank nanoparticles, suggesting that the encapsulated molecule partially shielded the surface while preserving overall stability (Figure 3A). The nanoparticles were mostly spherical, had a smooth surface morphology, were uniformly dispersed, and showed no signs of aggregation, according to an electron microscopy study (Figure 3B). The successful creation of well-defined chitosan-based nanoparticles was further confirmed by the measured particle size via microscopy, which agreed with DLS results.

By quantifying the amount of unencapsulated quercetin in the supernatant, encapsulation efficiency and drug loading were indirectly measured. Strong affinity between quercetin and the chitosan matrix was demonstrated by the excellent encapsulation effectiveness of quercetin-loaded chitosan nanoparticles. The drug loading capacity was adequate to allow for efficient administration while preserving the stability of the nanoparticles. These findings suggest that quercetin can be effectively encapsulated in chitosan nanoparticles via ionic gelation.

Quercetin encapsulation and interaction with chitosan were demonstrated at the molecular level by FTIR spectroscopy. Quercetin-loaded nanoparticles' FTIR spectra showed distinctive absorption bands that matched both chitosan and quercetin. The establishment of hydrogen bonding connections between quercetin hydroxyl groups and chitosan amino groups is suggested by the notable changes and expansion of the O–H and N–H stretching bands. Instead of just physical mixing, effective inclusion inside the polymeric network was further demonstrated by the attenuation of distinctive quercetin peaks (Figure 3C).

Studies on drug release *in vitro* revealed a biphasic release characteristic with a burst release at first, followed by a controlled and prolonged release of quercetin over time. Diffusion of quercetin from the chitosan matrix is reflected in the extended-release phase, while surface-associated quercetin is responsible for the initial release phase. The release data best suited the Higuchi and Korsmeyer-Peppas models, according to kinetic modeling, suggesting a diffusion-controlled release mechanism with polymer relaxation influencing drug release behavior (Figure 3D; Table 1). The formulated chitosan NPs also showed high yield, swelling index, and cumulative drug release (Table 2)

The improved physicochemical stability of quercetin following nano-encapsulation was further validated by thermal analysis. The distinctive melting endotherm of crystalline quercetin was either absent or broadened in the nanoparticle formulation, according to Differential Scanning Calorimetry (DSC) thermograms, indicating molecular dispersion of quercetin inside the chitosan matrix (Figure 3E). When compared to free quercetin, quercetin-loaded nanoparticles showed better thermal stability and a delayed commencement of thermal degradation, according to Thermogravimetric Analysis (TGA) (Figure 3F). These results suggest that quercetin's physicochemical robustness is improved, and it is shielded from thermal degradation by nano-encapsulation. The successful formulation of stable, uniformly sized quercetin-loaded chitosan nanoparticles with high encapsulation efficiency, controlled release behavior, and improved thermal stability is confirmed by these physicochemical characterization results taken together, supporting their use in targeted colorectal cancer therapy.

Cell viability assay

Using NCM460 normal colon epithelial cells as a non-malignant control, the antiproliferative effects of free quercetin, blank chitosan nanoparticles, and quercetin-loaded chitosan nanoparticles were assessed in HCT116 and HT-29 colorectal cancer cells (Figure 4A–C). While there was little cytotoxicity shown in normal cells, treatment with quercetin formulations clearly reduced the viability of cancer cells in a dose- and time-dependent manner. Free quercetin had mild cytotoxic effects on HCT116 cells, as seen in Figure 4A, with IC_{50} values of 62.4±3.8 μg/mL, 41.7±2.9 μg/mL, and 28.6±2.1 μg/mL at 24, 48, and 72 hours, respectively. Quercetin-loaded chitosan nanoparticles, on the other hand, greatly increased growth inhibition, resulting in significantly lower IC_{50} values of 34.9±2.6 μg/mL (24 h), 19.8±1.7 μg/mL (48 h), and 11.3±1.2 μg/mL (72 h) ($p<0.05$ against free quercetin at corresponding time intervals) (Table 3).

Similar trends were seen in HT-29 cells (Figure 4B), which generally showed somewhat lower sensitivity than HCT116 cells. At 24, 48, and 72 hours, free quercetin showed IC_{50} values of 71.2±4.5 μg/mL, 49.6±3.3 μg/mL, and 33.8±2.4 μg/mL, respectively. The cytotoxic efficacy was significantly enhanced by quercetin-loaded chitosan nanoparticles, which decreased IC_{50} values to 42.6±3.1 μg/mL (24 h), 24.7±2.0 μg/mL (48 h), and 14.9±1.5 μg/mL (72 h) ($p <0.05$) (Table 3). The biocompatibility of the carrier system was confirmed by the fact that blank chitosan nanoparticles showed no discernible cytotoxicity in either cancer cell type over the measured dose range. Crucially, after treatment, NCM460 normal colon epithelial cells maintained good vitality (Figure 4C). Cell viability remained above 80% even at the highest tested dose, demonstrating preferential toxicity towards malignant cells. Both free quercetin and quercetin-loaded nanoparticles demonstrated IC_{50} values surpassing 100 μg/mL at all time periods. All of these results show that quercetin's antiproliferative effect against colorectal cancer cells is greatly increased by nano-encapsulation, while normal colon epithelial cells are spared. The higher cellular absorption and prolonged intracellular drug release of quercetin-loaded chitosan nanoparticles are commensurate with their improved efficacy, offering a solid functional foundation for further mechanistic and *in vivo* studies.

Apoptosis and cell-cycle analysis

Flow cytometry was used to assess apoptosis and cell-cycle distribution in HCT116 and HT-29 colorectal cancer cells in order to explore the mechanism behind the increased cytotoxicity of quercetin-loaded chitosan nanoparticles (QCT-CSNPs) (Figure 5A–F). When cells treated with QCT-CSNPs were compared to free quercetin and blank chitosan nanoparticles, apoptosis examination using annexin V–FITC/Propidium Iodide (PI) labeling revealed a significant increase in early and late apoptotic populations (Figure 5A–C). Total apoptosis in HCT116 cells rose from 14.2±1.3% with free quercetin (50 μg/mL, 48 h) to 38.7±2.5% with QCT-CSNPs at the same concentration and time point ($p<0.05$). Similar trends were seen in HT-29 cells, where total apoptotic populations increased from 11.8±1.1% to 33.4±2.2% after nanoparticle treatment. Blank CSNPs caused very little apoptosis (less than 5%), demonstrating the biocompatibility of the carrier system. These results indicate that encapsulation of quercetin significantly enhances its pro-apoptotic effect in colorectal cancer cells.

QCT-CSNP administration caused G_2/M phase arrest in both HCT116 and HT-29 cells, according to cell-cycle analysis (Figure 5D–F). Following QCT-CSNP treatment, the percentage of cells in G_2/M in HCT116 cells increased from 18.6±1.5% in untreated controls to 42.3±2.8%, but free quercetin produced a lower increase to 28.1±2.0%. HT-29 cells showed a similar G_2/M arrest (control: 16.9±1.4%; QCT-CSNP: 39.1±2.5%). The observed reduction of proliferation and increased vulnerability to apoptosis are probably caused by this cell concentration at the G_2/M checkpoint. Together, these flow cytometry findings show that quercetin-loaded chitosan nanoparticles more successfully induce cell-cycle arrest and death than pure quercetin, which is in line with the lower IC_{50} values seen in the MTT assay (Figure 4A–C). The combination of increased absorption by cells, sus-

tained release, and targeted delivery provided by the nanoparticle formulation underlies these superior anticancer effects.

Quercetin-loaded CSNPs inhibit the RAS–PI3K–AKT–mTOR signaling axis in colorectal cancer cells

We used Western blotting and immunohistochemistry to examine the expression and activation status of important elements of the RAS–PI3K–AKT–mTOR pathway in HCT116 and HT-29 cells in order to clarify the molecular mechanisms underlying the increased cytotoxicity of Quercetin-loaded Chitosan Nanoparticles (QCT-CSNPs) (Figure 6A–D). When compared to free quercetin at equivalent dosages (50 µg/mL, 48 h), Western blot analysis showed that treatment with QCT-CSNPs considerably lowered total RAS protein levels and markedly decreased the phosphorylation of AKT (Ser473) and mTOR (Ser2448) (Figure 6A, B). In HCT116 cells treated with QCT-CSNPs, densitometric measurement, adjusted to β-actin, revealed a ~60% drop in p-AKT and ~55% reduction in p-mTOR compared to a ~30% reduction with free quercetin ($p<0.05$). HT-29 cells showed similar patterns, suggesting that nano-encapsulation significantly improves route inhibition. Equal protein loading was confirmed by the little drop in total PI3K levels and the stability of β-actin levels. The signaling profile was unaffected by blank chitosan nanoparticles, indicating that quercetin administration is responsible for the observed effects.

These results were confirmed in situ by immunohistochemical examination (Figure 6C & D). When compared to free quercetin, HCT116 and HT-29 cells treated with QCT-CSNPs showed significantly decreased immunoreactivity for RAS, p-AKT, and p-mTOR, as well as lower staining intensity and fewer positively labeled cells. The staining of cells treated with blank CSNPs was similar to that of controls. Significant decreases in RAS–PI3K–AKT–mTOR activity were confirmed by quantitative scoring of immunostaining ($p<0.05$). Crucially, the elevated apoptosis and G_2/M arrest shown by flow cytometry correspond with the reported suppression of this vital proliferative and survival pathway (Figure 5). A mechanistic explanation for the decreased IC_{20} values and selective anticancer action of QCT-CSNPs in the MTT experiment can be found in the downregulation of RAS and suppression of downstream AKT/mTOR phosphorylation (Figure 4). All of these findings suggest that quercetin's capacity to target the RAS–PI3K–AKT–mTOR axis is enhanced by nanoformulation, which disrupts oncogenic signaling and encourages programmed cell death in colorectal cancer cells.

Biodistribution analysis

To ascertain the systemic distribution and tumor-targeting effectiveness of quercetin-loaded chitosan nanoparticles in tumor-bearing mice, their *in vivo* biodistribution was examined. Following treatment, near-infrared whole-body fluorescence imaging demonstrated distinct temporal and spatial differences between quercetin-loaded chitosan nanoparticles and free quercetin (fluorescent probe). Animals given free fluorescent probe showed quick systemic distribution with strong early signals in highly perfused organs, especially the liver and kidneys, within 1-6 hours after treatment, according to IVIS imaging. By 24 hours, these signals had significantly decreased, suggesting quick clearance and little tumor retention. Mice given fluorescently labeled quercetin-loaded chitosan nanoparticles, on the other hand, showed a persistent fluorescence signal over time, gradually building up near the tumor location. Interestingly, tumor-associated fluorescence appeared as early as 6 hours after treatment, peaked at 24 hours, and persisted for 48 hours, indicating extended circulation and improved tumor retention of the nanoparticle formulation (Figure 7A-D).

At all time periods after 6 hours, mice treated with quercetin-loaded chitosan nanoparticles had considerably higher fluorescence intensity within their tumors than those treated with free quercetin, according to quantitative Region-of-Interest (ROI) analysis ($p<0.05$) (Figure 7A). These results were further supported by *ex vivo* fluorescence imaging of removed organs at the terminal time point. While free quercetin is primarily localized to the liver and kidneys, which is consistent with quick hepatic metabolism and renal clearance, tumor tissues from the nanoparticle-treated group showed noticeably increased fluorescence intensity (Figure 7C & D). The tumor-to-organ fluorescence ratio was much higher for quercetin-loaded chitosan nanoparticles than for pure quercetin, even though some nanoparticle-associated fluorescence was seen in the liver and spleen, indicating absorption by the reticuloendothelial system (Figure 7D). The chitosan-based carrier's nanoscale size, positive surface charge, and extended systemic circulation are responsible for this increased tumor accumulation. These factors work together to enable passive tumor targeting through the Enhanced Permeability and Retention (EPR) effect.

Overall, the biodistribution results show that quercetin's *in vivo* delivery profile is significantly improved by chitosan-mediated nano-encapsulation, which promotes preferred tumor accumulation, decreased off-target distribution, and sustained retention at the tumor site. These results underpin the improved anticancer activity observed in subsequent therapeutic and mechanistic investigations and provide compelling *in vivo* evidence for the higher delivery efficiency of quercetin-loaded chitosan nanoparticles.

Experimental animals and ethical consideration

Throughout the trial, every animal maintained its health, and no procedure-related deaths were noted. The mice's activity, grooming, and food habits were all typical, and the housing circumstances were well tolerated. No unanticipated adverse effects were noted during tumor induction, oral therapy, or terminal procedures, and all experimental interventions adhered to institutional ethical guidelines.

Tumor xenograft establishment

All animals that received a subcutaneous injection of HCT116 cells had effective tumor engraftment. Within 9 days of inoculation, palpable tumors appeared and grew steadily. With little variation between animals, tumors achieved the predetermined treatment initiation volume of roughly 100–120 mm^3, allowing for consistent randomization into treatment groups. Over the course of the study, tumor growth in vehicle-treated mice followed an exponential trend, demonstrating the xenograft model's resilience (Figure 8).

Effect of oral treatments on tumor growth

When quercetin-loaded chitosan nanoparticles were administered orally, tumor development was significantly suppressed in comparison to vehicle control, free quercetin, and blank chitosan nanoparticle groups. In mice treated with quercetin-loaded nanoparticles, tumor volume assessments showed a time-dependent reduction of tumor development, with significant differences starting on day 12 ($p<0.05$). Mice given quercetin-loaded chitosan nanoparticles showed the biggest decrease in tumor weight and volume at the conclusion of the 21-day treat-

ment period. When compared to the vehicle control, the anticancer impact of free quercetin was somewhat but significantly lower, and the growth of tumors was not significantly affected by blank chitosan nanoparticles (Figure 9). These results suggest that quercetin's oral anticancer effectiveness is significantly increased by nano-encapsulation.

Body weight and oral tolerability

Over the course of the trial, body weight monitoring showed no discernible variations between treatment groups. When quercetin-loaded chitosan nanoparticles were administered to mice, body weights remained constant, similar to those of the vehicle and blank nanoparticle controls. Additionally, there was no discernible weight loss following free quercetin administration. Good oral tolerability is shown by the lack of treatment-related weight loss, which also implies that the anticancer effects were not linked to systemic toxicity (Figure 10A). As shown in Figure 10B, oral administration of quercetin-loaded chitosan nanoparticles resulted in a pronounced reduction in final tumor weight compared with all other groups. Mice treated with quercetin-loaded chitosan nanoparticles exhibited a significant decrease in tumor mass relative to vehicle control (**p<0.01**), indicating enhanced antitumor efficacy. Free quercetin also produced a moderate but significant reduction in tumor weight compared with the vehicle group (*p<0.05*), whereas blank chitosan nanoparticles did not elicit a significant effect. These results demonstrate that chitosan-based nano-encapsulation markedly potentiates the *in vivo* antitumor activity of quercetin following oral administration (Figure 10A & B).

Terminal tumor characteristics and tissue collection

At study termination, tumors excised from quercetin-loaded chitosan nanoparticle–treated mice were visibly smaller and weighed significantly less than those from control and free quercetin groups ($p<0.05$). Excised tumor tissues were of uniform consistency and suitable for downstream molecular analyses. Tumors and major organs were successfully processed for Western blotting, immunohistochemistry, and histopathological evaluation, enabling a comprehensive assessment of therapeutic efficacy and the mechanism of action (Figure 11A-D).

Toxicity evaluation of quercetin-loaded chitosan nanoparticles

No overt signs of systemic toxicity were observed in any treatment group during the study period. Daily monitoring revealed normal behavior, feeding, and grooming patterns in mice treated with quercetin-loaded chitosan nanoparticles. Body weight trajectories remained comparable across all groups. Serum biochemical analyses demonstrated that hepatic (ALT, AST) and renal (urea, creatinine) function parameters in quercetin-loaded nanoparticle–treated mice remained within normal physiological ranges and did not differ significantly from vehicle or blank nanoparticle controls. Free quercetin treatment also did not induce clinically relevant biochemical alterations (Figure 12). Histopathological examination of major organs, including the liver, kidneys, heart, lungs, and spleen, revealed preserved tissue architecture with no evidence of inflammation, necrosis, or degenerative changes in mice treated with quercetin-loaded chitosan nanoparticles (Figure 13). These findings indicate that nano-encapsulation did not elicit detectable organ toxicity and may mitigate potential systemic adverse effects associated with free quercetin administration.

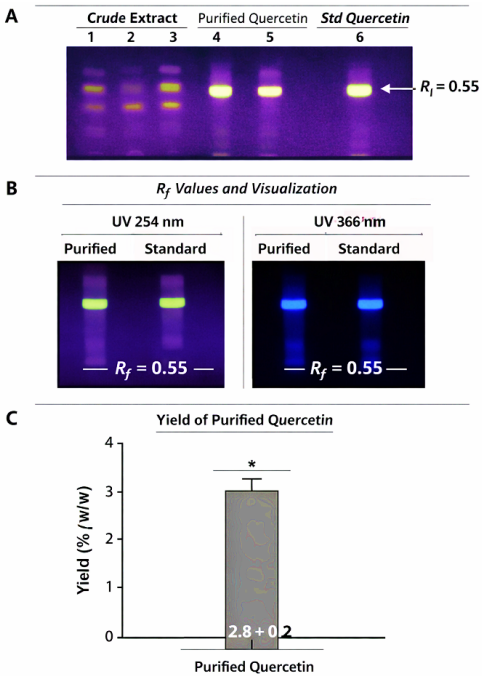

Figure 1: Isolation and purification of quercetin from plant extract. **(A)** TLC profile of crude extract and purified fractions. Lanes 1–3: Crude extract fractions showing multiple spots under UV light (254 nm). Lanes 4–5: Pooled fractions after column chromatography, showing a single spot corresponding to quercetin. Lane 6: Standard quercetin ($R_f \approx 0.55$). **(B)** R_f values and visualization under UV (254 and 366 nm). R_f values for the purified fractions matched the standard quercetin. **(C)** Yield of purified quercetin. Bar graph showing the mean yield of quercetin from three independent extractions (2.8±0.2% w/w).

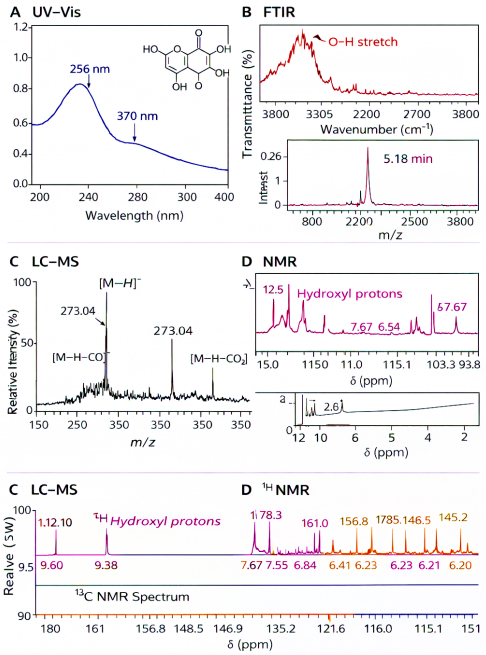

Figure 2: Characterization of isolated quercetin by spectroscopic and spectrometric techniques. (A) UV–Vis spectrum showing absorption maxima at 256 nm and 370 nm, characteristic of the flavonol structure. **(B) FTIR spectrum** highlighting O–H stretching (~3400 cm^{-1}), C=O stretching (~1660 cm^{-1}), and aromatic C=C vibrations (1600–1450 cm^{-1}). **(C) LC–MS spectrum** obtained in negative ESI mode, showing molecular ion peak at m/z 301.03 $[M–H]^-$ and major fragment ions corresponding to CO and CO_2 losses. **(D) NMR spectra (^1H and ^{13}C)** showing aromatic proton signals (δ 6.2–7.7 ppm), phenolic hydroxyl protons (δ 9.0–12.5 ppm), and corresponding ^{13}C resonances, confirming the structure of quercetin.

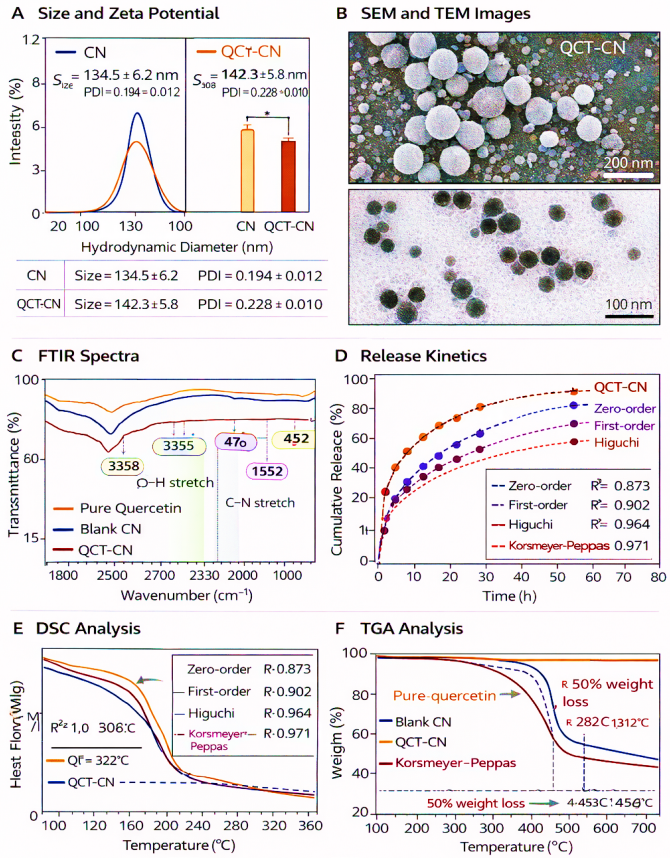

CN	Size = 134.5 ± 6.2	PDI = 0.194 ± 0.012
QCT-CN	Size = 142.3 ± 5.8	PDI = 0.228 ± 0.010

Figure 3: Physicochemical characterization of quercetin-loaded chitosan nanoparticles. **(A)** Particle size distribution by Dynamic Light Scattering (DLS). The hydrodynamic diameter of quercetin-loaded chitosan nanoparticles was determined by DLS, showing a narrow and unimodal size distribution indicative of uniform nanoparticle formation. **(B)** Zeta potential analysis. Zeta potential measurements demonstrated a positive surface charge for quercetin-loaded chitosan nanoparticles, reflecting protonated amino groups of chitosan and indicating good colloidal stability. **(C)** Morphological analysis by electron microscopy (SEM/TEM). Electron micrographs revealed predominantly spherical nanoparticles with smooth surface morphology and minimal aggregation, confirming nanoscale size and uniform dispersion. **(D)** FTIR spectra of quercetin, blank chitosan nanoparticles, and quercetin-loaded chitosan nanoparticles. FTIR analysis showed characteristic absorption bands corresponding to quercetin and chitosan. Shifts and broadening of O–H and N–H stretching vibrations in the loaded nanoparticles indicate intermolecular interactions, confirming successful encapsulation of quercetin within the chitosan matrix. **(E)** In vitro release profile and release kinetics of quercetin. Cumulative release of quercetin from chitosan nanoparticles in phosphate-buffered saline (pH 7.4) at 37°C demonstrated a biphasic release pattern with an initial burst followed by sustained release. Kinetic fitting supported a diffusion-controlled release mechanism. **(F)** Differential Scanning Calorimetry (DSC) thermograms. DSC analysis showed the disappearance or broadening of the characteristic melting peak of crystalline quercetin in the nanoparticle formulation, indicating molecular dispersion and reduced crystallinity after encapsulation. **(G)** Thermogravimetric Analysis (TGA). TGA profiles revealed enhanced thermal stability of quercetin-loaded chitosan nanoparticles compared with free quercetin, with delayed onset of thermal degradation and reduced weight loss.

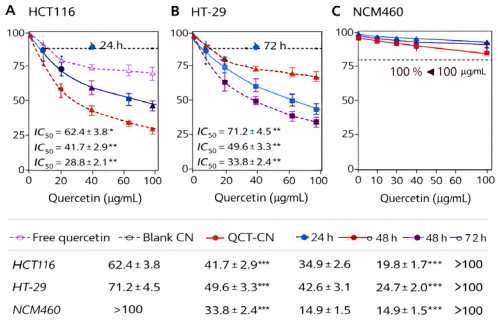

HCT116	62.4 ± 3.8	41.7 ± 2.9***	34.9 ± 2.6	19.8 ± 1.7***	>100
HT-29	71.2 ± 4.5	49.6 ± 3.3***	42.6 ± 3.1	24.7 ± 2.0***	>100
NCM460	>100	33.8 ± 2.4***	14.9 ± 1.5	14.9 ± 1.5***	>100

Figure 4: Dose–response analysis of quercetin cytotoxicity in colorectal cancer and normal colon epithelial cells. **(A)** HCT116 cells: Cell viability after treatment with free quercetin, blank Cchitosan Nanoparticles (CN), and Quercetin-loaded Chitosan Nanoparticles (QCT-CN) at concentrations of 5–100 µg/mL for 24, 48, and 72 h. Quercetin-loaded CSNPs demonstrated significantly enhanced cytotoxicity, with IC_{50} values of 34.9 ± 2.6 µg/mL (24 h), 19.8±1.7 µg/mL (48 h), and 11.3±1.2 µg/mL (72 h), compared with free quercetin. **(B)** HT-29 cells: Similar dose- and time-dependent reduction in cell viability was observed, with quercetin-loaded CS-NPs IC_{50} values of 42.6±3.1 µg/mL (24 h), 24.7±2.0 µg/mL (48 h), and 14.9±1.5 µg/mL (72 h). Free quercetin exhibited higher IC_{50} values at all time points. **(C)** NCM460 normal colon epithelial cells: High cell viability was maintained (>80%) after treatment with both free quercetin and quercetin-loaded CSNPs, indicating selective cytotoxicity toward cancer cells. Blank CSNPs did not significantly affect viability in any cell line. Data are presented as mean ± SD (n=3). Statistical significance between free quercetin and quercetin-loaded CSNPs at each time point is indicated by ***P<0.05 (one-way ANOVA with Tukey's post hoc test).

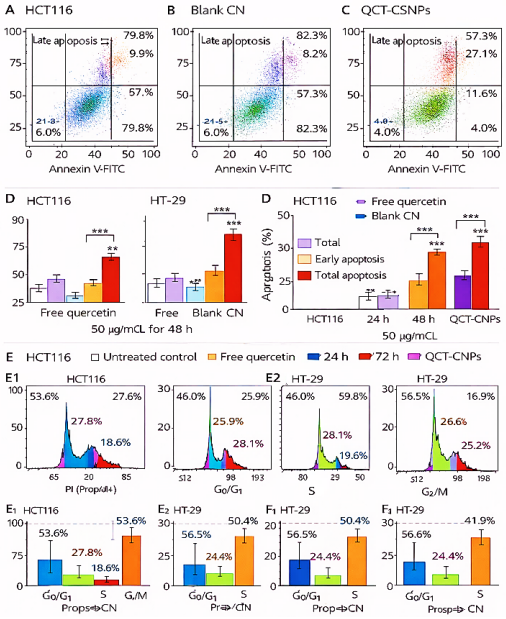

Figure 5: Apoptosis and cell-cycle analysis of colorectal cancer cells treated with quercetin-loaded chitosan nanoparticles. **(A–C)** Flow cytometry dot plots of HCT116 and HT-29 cells following treatment with free quercetin, blank Chitosan Nanoparticles (CN), and quercetin-loaded CSNPs (50 µg/mL, 48 h). Quadrants indicate viable (Annexin V^-/PI^-), early apoptotic (Annexin V^+/PI^-), late apoptotic (Annexin V^+/PI^+), and necrotic cells (Annexin V^-/PI^+). Quercetin-loaded CSNPs induced significantly higher total apoptosis than free quercetin ($p<0.05$). **(D–F)** Quantification of apoptotic populations and cell-cycle distribution. PI-stained histograms show G_0/G_1, S, and G_2/M phase percentages. Treatment with QCT-CSNPs caused marked G_2/M arrest in both HCT116 and HT-29 cells compared with free quercetin and blank CSNPs. Data represent mean±SD (n=3); statistical significance versus free quercetin indicated by **$p<0.05$ and ***p<0.01 (one-way ANOVA, Tukey's post hoc test).

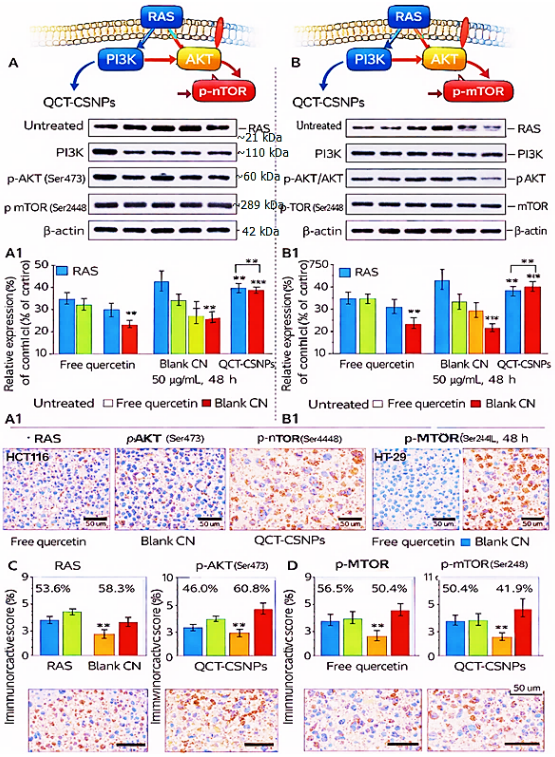

Figure 6: Quercetin-loaded CSNPs inhibit the RAS–PI3K–AKT–mTOR signaling pathway in colorectal cancer cells. **(A,B)** Western blot analysis of HCT116 (A) and HT-29 **(B)** cells treated with free quercetin, blank chitosan nanoparticles (CN), or quercetin-loaded CSNPs (50 μg/mL, 48 h). Blots show total RAS, PI3K, phosphorylated AKT (p-AKT, Ser473), phosphorylated mTOR (p-mTOR, Ser2448), and β-actin as loading control. Densitometric quantification (A1, B1) shows the relative percentage of expression normalized to β-actin. Quercetin-loaded CSNPs significantly reduce p-AKT, p-mTOR, and RAS compared with free quercetin (**p<0.05). **(C,D)** Immunohistochemistry of HCT116 **(C)** and HT-29 **(D)** cells. Panels show staining for RAS, p-AKT, and p-mTOR in cells treated as indicated. Colored arrows highlight reduced immunoreactivity following QCT-CSNP treatment. Scale bars: 50 μm. Quantitative scoring of immunoreactivity confirms significant inhibition of the RAS–PI3K–AKT–mTOR pathway (***p<0.01 vs. free quercetin). Data represent mean ± SD (n=3 independent experiments). Blank CSNPs exhibit minimal effect on signaling, confirming the specificity of quercetin delivery by nanoparticles.

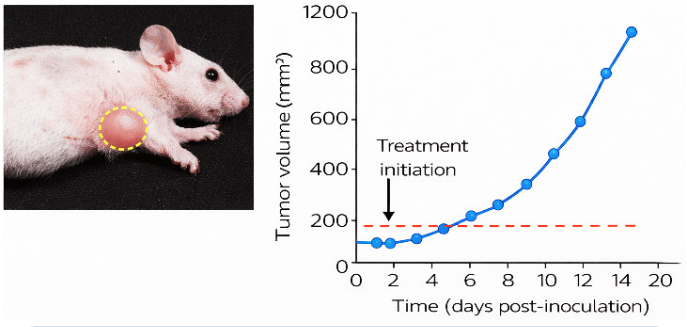

Figure 8: Tumor xenograft formation. Subcutaneous inoculation of HCT116 cells in BALB/c nude mice resulted in successful tumor engraftment, with the tumor reaching the predefined treatment initiation volume approximately 100-120 mm³. The encircled part (arrow) of the animal indicates an externally formed solid tumor.

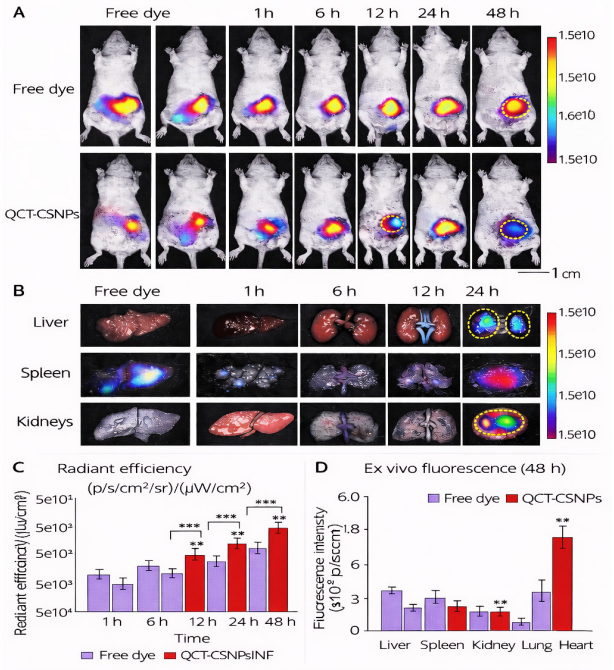

Figure 7: *In vivo* biodistribution and tumor accumulation of quercetin-loaded CSNPs. **(A)** Whole-body IVIS fluorescence images of tumor-bearing mice following administration of free fluorescent dye or fluorescently labeled Quercetin-loaded Chitosan Nanoparticles (QCT-CSNPs). Images were acquired at 1, 6, 12, 24, and 48 h post-administration using identical excitation and emission settings. The scale indicates fluorescence intensity (radiant efficiency). QCT-CSNP–treated animals show sustained systemic circulation and progressive tumor accumulation, in contrast to the rapid clearance of free dye. **(B)** *Ex vivo* fluorescence imaging of excised major organs (liver, spleen, kidneys, lungs, heart) and tumor tissues at 48 h post-administration. Strong tumor-associated fluorescence is evident in the QCT-CSNP group, whereas free dye predominantly localizes to clearance organs. Scale bars represent 1 cm. **(C)** Quantitative Region-Of-Interest (ROI) analysis of fluorescence intensity expressed as **radiant efficiency (p/s/cm²/sr)/(μW/cm²)** for tumors and major organs at 48 h post-administration. Data are presented as mean ± SD (n=6). Quercetin-loaded chitosan nanoparticles exhibit significantly higher tumor accumulation and tumor-to-organ fluorescence ratios compared with free dye ($p<0.05$).

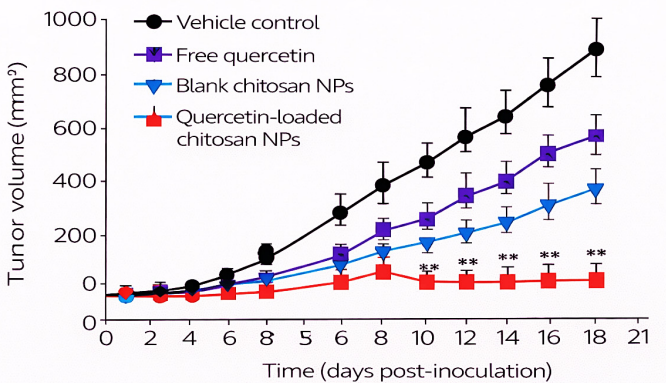

Figure 9: Effect of oral treatment on tumor growth. Oral administration of quercetin-loaded CSNPs significantly (**p<0.05; one-way ANOVA) suppressed tumor growth compared with vehicle control, free quercetin, and blank CSNPs.

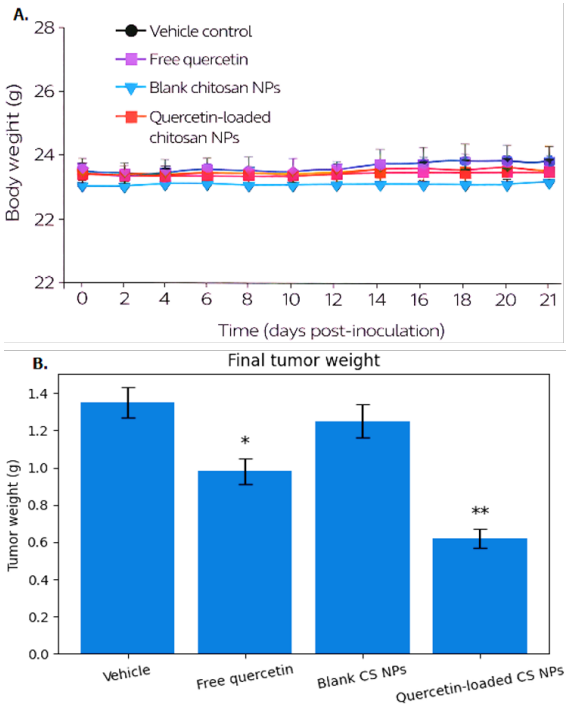

Figure 10: (A) Body weight and oral tolerability. **(B)** Final weights of tumor in induced mice. Body weight monitoring demonstrated no significant differences among treatment groups throughout the experimental period. Mice treated with quercetin-loaded CSNPs maintained stable body weights, comparable to those of vehicle and blank nanoparticle controls. *Data are presented as mean±SE (n=6). Statistical significance was determined by one-way ANOVA followed by post hoc analysis. *p<0.05, **p<0.01 compared with vehicle control.*

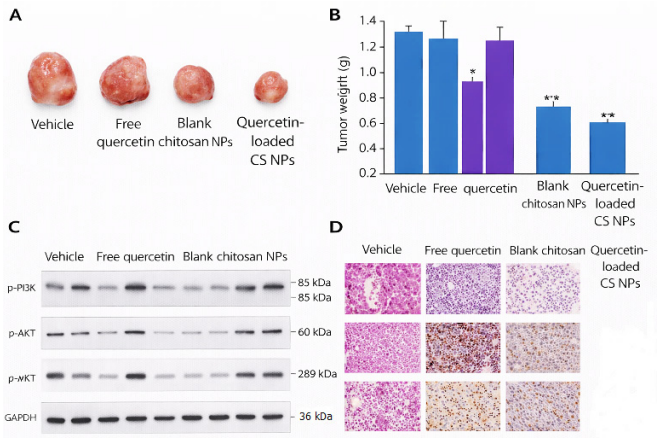

Figure 11: Terminal tumor characteristics and molecular analysis following oral treatment. (A) Representative images of excised tumors collected at the end of the 21-day treatment period from vehicle control, free quercetin, blank Chitosan Nanoparticles (CS NPs), and quercetin-loaded CS NPs–treated mice, showing a marked reduction in tumor size in the nano-formulation group. **(B)** Quantitative analysis of final tumor weight demonstrates a significant decrease in tumors from quercetin-loaded CS NP–treated mice compared with vehicle, free quercetin, and blank CS NP groups ($p<0.05$). Data are expressed as mean ± SEM (n=6). **(C)** Western blot images of tumor tissues illustrating modulation of key proteins in the RAS–PI3K–AKT–mTOR signaling pathway following treatment. Molecular weights (kDa) of each protein are indicated alongside the bands, with GAPDH used as the loading control. **(D)** Schematic overview of tumor and organ collection at study termination for downstream analyses, including Western blotting, immunohistochemistry, and histopathological evaluation, confirming the suitability of excised tissues for mechanistic and toxicity assessments.

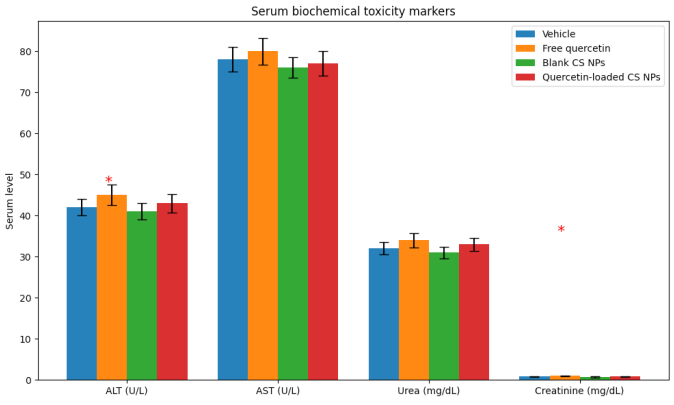

Figure 12: Effects of quercetin-loaded CSNPs on serum biomarkers of induced-mice models. Results are mean±SD (n=6 mice per group). * Statistically significant at p<0.05 (one-way ANOVA).

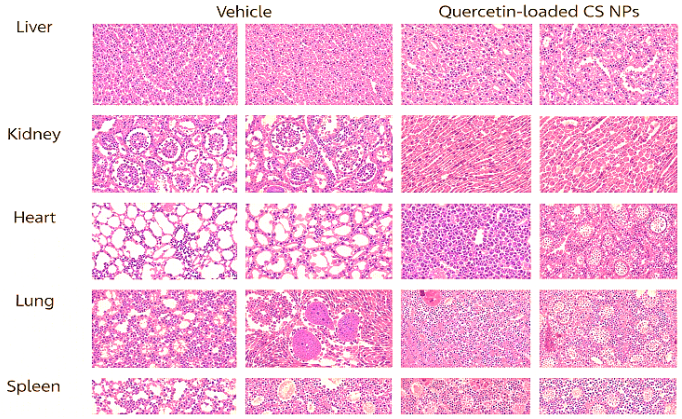

Figure 13: Histopathological evaluation of major organs following oral administration of quercetin-loaded chitosan nanoparticles. Hematoxylin and Eosin (H&E)–stained sections of the liver, kidneys, heart, lungs, and spleen were collected at the end of the treatment period. Tissues from mice treated with quercetin-loaded chitosan nanoparticles show preserved histoarchitecture with normal cellular organization and no detectable signs of inflammation, necrosis, or degenerative alterations, comparable to control groups. These findings indicate good systemic biocompatibility and absence of overt organ toxicity following oral nano-formulated quercetin treatment. Scale bar=50 µm.

Table 1: *In vitro* drug release kinetics of quercetin from chitosan nanoparticles.

Kinetic model	Equation	Kinetic parameters	R^2 value
Zero-order	$Qt = Q0 + k0t$	$k0 = 1.12\ \%\cdot h^{-1}$	0.873
First-order	$\ln(1 - Qt/Q\infty) = -k1t$	$k1 = 0.045\ h^{-1}$	0.902
Higuchi	$Qt = kH\sqrt{t}$	$kH = 8.76\ \%\cdot h^{-½}$	0.964
Korsmeyer–Peppas	$Qt/Q\infty = kKP\cdot t^{n}$	kKP = 0.62, n = 0.48	0.971

In vitro release data were fitted to zero-order, first-order, Higuchi, and Korsmeyer–Peppas kinetic models. The Higuchi and Korsmeyer–Peppas models showed the highest correlation coefficients (R^2), indicating a predominantly diffusion-controlled release mechanism. The release exponent *n* (<0.5) further suggests Fickian diffusion of quercetin from the chitosan matrix.

Table 2: Physicochemical properties and pH-dependent release behavior of quercetin-loaded chitosan nanoparticles
Values are expressed as mean ± SD (n=3). Different superscript letters ([a]–[c]) within the cumulative drug release parameter indicate statistically significant differences between pH conditions (p<0.05, one-way ANOVA followed by Tukey's post hoc test).

Parameter	Condition	Value
Yield (%)	Post-formulation	78.4 ± 3.1
Swelling index (%)	PBS, pH 7.4	62.7 ± 4.5
Encapsulation efficiency (%)	Quercetin-CSNPs	84.2 ± 2.6
Drug loading (%)	Quercetin-CSNPs	18.9 ± 1.3
Cumulative drug release (%)	pH 1.2 (2 h)	22.4 ± 2.1[a]
	pH 6.8 (8 h)	55.8 ± 3.4[b]
	pH 7.4 (24 h)	81.6 ± 4.2[c]

Table 3: IC_{50} values (μg/mL) of free quercetin and quercetin-loaded chitosan nanoparticles in colorectal cancer and normal colon cell lines.

Cell line	Treatment	24 h	48 h	72 h
HCT116	Free quercetin	62.4±3.8	41.7±2.9	28.6±2.1
	Quercetin-loaded CSNPs	34.9±2.6*	19.8±1.7*	11.3±1.2*
HT-29	Free quercetin	71.2±4.5	49.6±3.3	33.8±2.4
	Quercetin-loaded CSNPs	42.6±3.1*	24.7±2.0*	14.9±1.5*
NCM460	Free quercetin	>100	>100	>100
	Quercetin-loaded CSNPs	>100	>100	>100

Values are expressed as mean ± SD (n=3). *P<0.05 compared with free quercetin at the corresponding time point using one-way ANOVA followed by Tukey's post hoc test.
CSNPs: chitosan nanoparticles.

Discussion

The current study shows that by improving quercetin's physicochemical stability, oral bioavailability, tumor accumulation, and molecular suppression of the RAS–PI3K–AKT–mTOR signaling axis, chitosan-based nano-encapsulation significantly increases the anticancer efficacy of quercetin against colorectal cancer. This study offers strong preclinical evidence for the development of quercetin-loaded chitosan nanoparticles as an oral phytomedicine-based anticancer strategy through an integrated approach combining formulation science, in vitro cellular assays, mechanistic pathway analyses, biodistribution profiling, and *in vivo* therapeutic evaluation.

Although quercetin's anticancer potential is well known, its quick metabolic breakdown, poor water solubility, and minimal systemic exposure after oral administration have hindered its practical translation. By encasing quercetin in a stable nanoscale carrier with a desirable particle size, low polydispersity, and a positive surface charge, ionic gelation-derived chitosan nanoparticles effectively overcame these limitations in this investigation. These characteristics are essential for improved epithelial absorption, mucosal adhesion, and gastrointestinal stability—aspects that are especially pertinent to colorectal cancer treatment. Effective quercetin incorporation into the chitosan matrix and enhanced thermal and physicochemical stability were validated by FTIR, DSC, and TGA studies, suggesting that quercetin is shielded from premature breakdown by nano-encapsulation.

Physicochemical analyses confirmed the successful formulation of quercetin-loaded chitosan nanoparticles with nanoscale size, narrow polydispersity, and a positive surface charge, all of which are desirable attributes for oral delivery and intestinal uptake. The observed zeta potential supports electrostatic stability and mucoadhesive interactions with the gastrointestinal epithelium, consistent with earlier reports showing that chitosan-based carriers improve oral absorption of polyphenols and flavonoids [25,48]. FTIR, DSC, and TGA data collectively indicated molecular-level interactions between quercetin and the chitosan matrix, reduced crystallinity, and enhanced thermal stability, corroborating previous studies that reported improved physicochemical stability of flavonoids following nano-encapsulation [48]. Moreover, the sustained release behavior and favorable release kinetics align with earlier findings that chitosan nanoparticles provide controlled drug release under physiological conditions, thereby prolonging systemic exposure [50].

The system's appropriateness for oral delivery is further supported by the prolonged release profile of quercetin from chitosan nanoparticles under physiological settings. Diffusion-controlled and anomalous release pathways were revealed by kinetic modeling [51], enabling extended exposure of tumor cells to therapeutically appropriate quercetin concentrations. When compared to free quercetin, this persistent release behavior probably explains the better antiproliferative effects seen both *in vitro* and *in vivo*.

Quercetin-loaded chitosan nanoparticles exhibited markedly increased cytotoxicity against colorectal cancer cells at the cellular level, but they spared normal colonic epithelial cells. An increased therapeutic index is demonstrated by the decreased IC_{50} values, as well as the marked induction of apoptosis and G_0/G_1 cell-cycle arrest. Crucially, the coordinated suppression of the RAS–PI3K–AKT–mTOR pathway—a key oncogenic signaling axis that is frequently dysregulated in colorectal cancer—was mechanistically connected to these cellular effects [6,7,45]. The ability of nanocarrier systems to improve intracellular drug delivery and get around signaling redundancy was demonstrated by Western blot and immunohistochemical analyses, which verified that nano-encapsulated quercetin more successfully suppressed RAS expression and downstream phosphorylation of AKT and mTOR compared with free quercetin. These findings agree with multiple reports demonstrating that nanoparticle-mediated delivery amplifies the anticancer potency of quercetin by improving intracellular accumulation and cellular uptake [25,52,53]. The induction of apoptosis and cell-cycle arrest observed in this study is consistent with earlier mechanistic studies describing quercetin-induced G0/G1 or G2/M arrest and activation of intrinsic apoptotic pathways [46,54,55]. Notably, the magnitude of apoptotic induction achieved by the nano-formulation exceeded that reported for free quercetin in comparable *in vitro* systems, highlighting the advantage of nanoparticle-assisted delivery.

Mechanistically, the present data show that quercetin-loaded chitosan nanoparticles effectively suppress the RAS–PI3K–AKT–mTOR signaling axis, as demonstrated by Western blot and immunohistochemical analyses. Downregulation of PI3K, phosphorylated AKT, and mTOR signaling components is in agreement with prior studies identifying this pathway as a critical molecular target of quercetin in colorectal and other cancers [56,57]. However, the more pronounced inhibition observed here suggests that nano-encapsulation enhances pathway modulation, likely through sustained tumor exposure and

improved bioavailability. Importantly, these results support and extend earlier *in vitro* observations by confirming pathway inhibition in an in vivo tumor context following oral administration, which has been less frequently demonstrated.

The nano-formulation's delivery advantage was further supported by biodistribution experiments. Comparing quercetin-loaded chitosan nanoparticles to free dye, fluorescence imaging demonstrated longer systemic retention, preferential tumor accumulation, and decreased exposure to off-target organs, better oral absorption, the mucoadhesive qualities of chitosan, and passive accumulation through the increased permeability and retention (EPR) effect are probably responsible for this better tumor localization. The greater tumor growth inhibition seen in the xenograft model was closely connected with these biodistribution features.

Going further, the enhanced tumor localization observed may be attributed to prolonged circulation, improved intestinal uptake, and passive tumor targeting, collectively contributing to superior therapeutic outcomes. Correspondingly, *in vivo* antitumor efficacy studies showed significant tumor growth suppression and reduced terminal tumor weight in nanoparticle-treated mice, exceeding the effects of free quercetin. These findings align with earlier reports of quercetin nano-formulations but are particularly notable because they were achieved via oral administration, reinforcing the translational relevance for phytomedicine-based interventions.

Oral treatment of quercetin-loaded chitosan nanoparticles effectively inhibited tumor development and decreased final tumor weight without causing systemic toxicity, according to *in vivo* effectiveness tests. The biocompatibility and safety of the nano-formulation were proven by body weight stability, retained organ histology, and normal biochemical indicators. The therapeutic benefit of this delivery method was further highlighted by the noteworthy fact that nano-encapsulation seems to reduce any possible negative effects connected with free quercetin.

Notwithstanding the encouraging results, it is important to recognize several limits. In this work, tumor heterogeneity across various genetic backgrounds was not investigated because only one colorectal cancer xenograft model was used. Furthermore, thorough pharmacokinetic characterization of quercetin after oral nano-administration was outside the purview of our investigation, even if molecular pathway alteration was shown. Comprehensive pharmacokinetic and metabolic assessments, comparisons with various CRC models, and evaluations of long-term safety should all be part of future research. Additionally, investigating combination tactics with specific inhibitors or conventional chemotherapeutic treatments may uncover synergistic effects and aid in the fight against drug resistance. Clinical translation will also need to evaluate batch-to-batch repeatability and scaling up nanoparticle production.

This study presents a logical approach to using nanotechnology to update conventional plant-derived medicines from a phytomedicine standpoint. Because it is consistent with traditional usage paradigms and patient compliance, oral administration is still the most preferred method for phytochemicals. Chitosan-based nano-delivery systems provide a workable way to overcome the long-standing translational obstacles linked to flavonoids like quercetin by enhancing oral bioavailability, tumor targeting, and molecular selectivity. Quercetin-loaded chitosan nanoparticles are positioned as a prospective candidate for further development as an auxiliary or alternative therapy option in the management of colorectal cancer due to their shown suppression of a clinically relevant oncogenic pathway and excellent safety profile.

Conclusion

This study concludes by showing that quercetin's therapeutic potential against colorectal cancer is greatly increased by chitosan-based nano-encapsulation. In comparison to free quercetin, quercetin-loaded chitosan nanoparticles demonstrated greater antiproliferative and pro-apoptotic effects by enhancing physicochemical stability, oral bioavailability, and tumor targeting. The nano-formulation demonstrated a good safety profile after oral treatment by successfully inhibiting colorectal tumor development in animals without causing systemic harm. Cellular, molecular, and histological investigations verified that the improved anticancer activity was mechanistically tightly linked to coordinated suppression of the RAS–PI3K–AKT–mTOR signaling axis. The ability of chitosan nanoparticles to overcome important translational constraints of phytochemicals is highlighted by the integration of sustained drug release, enhanced biodistribution, and tailored pathway modulation. All things considered; these results lend credence to the possibility of quercetin-loaded chitosan nanoparticles as a sensible, oral phytomedicine-based treatment approach for colorectal cancer. In order to move nanostructured plant-derived drugs closer to clinical use, the work offers a solid preclinical basis for additional pharmacokinetic, combinatorial, and translational research.

Author declarations

CRediT authorship contribution statement

Cletus Anes Ukwubile: Conceptualization, Writing – original draft, Methodology, Investigation, Formal analysis, Data curation, Supervision. Babagana Modu: Formal analysis, Data curation. Methodology, Investigation, Visualization, Writing – review & editing. Hassan Braimah Yesufu: Resources, Methodology, Formal analysis, Project administration, Supervision, Writing – review & editing. Sumaila Mejida: Formal analysis, Data curation, Writing – review & editing. Emmanuel Oise Ikpefan: Writing – review & editing, Formal analysis, Data curation, Funding acquisition.

Declaration of competing interest

We have none to declare.

Ethical considerations

The animals used in this study were approved by the Animal Research Ethics Committee (AREC) of the Department of Pharmacology and Toxicology, Faculty of Pharmacy, University of Maiduguri, with approval number FP/03/24/SP.9788.

Acknowledgments

We are grateful to Prof. H. Nettey, University of Ghana, Legon, Accra, Ghana, for his support in this work.

Funding

The authors received no funding for this work.

Data availability

Data will be made available on genuine request.

References

1. Liu Y, Li Q, Tang D, Li M, Zhao P, Yang W, et al. SNHG17 promotes the proliferation and migration of colorectal adenocarcinoma cells by modulating CXCL12-mediated angiogenesis. Cancer Cell Int. 2020; 20: 1-10.
2. Ojo OA, Adeyemo TR, Rotimi D, Batiha GES, Mostafa-Hedeab G, Iyobhebhe ME, et al. Anticancer properties of curcumin against colorectal cancer: A review. Front Oncol. 2022; 12: 1-13.
3. Hossain MS, Karuniawati H, Jairoun AA, Urbi Z, Ooi DJ, John A, et al. Colorectal cancer: A review of carcinogenesis and global burden. Cancer. 2022; 14: 1-25.
4. Prakash A, Rubin N, Staley C, Onyeaghala G, Wen YF, Shaukat A, et al. Effect of ginger supplementation on the fecal microbiome in subjects with prior colorectal adenoma. Sci Rep. 2024; 14: 1-9.
5. Jamieson S, Butzow R, Andersson N, Alexiadis M, Unkila-Kallio L, Heikinheimo M, et al. The FOXL2 C134W mutation is characteristic of adult granulosa cell tumors of the ovary. Mod Pathol. 2010; 23: 1477-1485.
6. Song ZG, Liu YS, Dai SS, Yin ST, Zeng YD, Liu YC, et al. The integration strategy of Didang decoction against cerebral ischemia-reperfusion injury: Regulation of apoptosis-autophagy-inflammation network and validation of PI3K/Akt pathway. J Ethnopharmacol. 2025; 353: 120277.
7. Wang H, Wu B, Wang H. Alpha-hederin induces the apoptosis of oral cancer SCC-25 cells by regulating PI3K/Akt/mTOR signaling pathway. Electron J Biotechnol. 2019; 38: 27-31.
8. Zouhri A, Bouddine T, El Menyiy N, Kachkoul R, El Y, Siddique F, et al. Ionomic analysis, polyphenols characterization, analgesic, anti-inflammatory and antioxidant capacities of Cistus laurifolius leaves: In vitro, in vivo, and in silico investigations. Sci Rep. 2023; 13: 1-17.
9. Azarmehr N, Afshar P, Moradi M, Sadeghi H, Sadeghi H, Alipoor B, et al. Hepatoprotective and antioxidant activity of watercress extract on acetaminophen-induced hepatotoxicity in rats. Heliyon. 2019; 5: e02072.
10. Bencheikh N, Ouahhoud S, Cordero MAW, Alotaibi A, Fakchich J, Ouassou H, et al. Nephroprotective and antioxidant effects of flavonoid-rich extract of Thymelaea microphylla Coss. et Dur aerial part. Appl Sci. 2022; 12: 9272.
11. AlMousa LA, Pandey P, Lakhanpal S, Kyada AK, Malathi H, Nayak PP, et al. An updated review deciphering the anticancer potential of pentacyclic triterpene lupeol and its nanoformulations. Front Pharmacol. 2025; 16: 1-20.
12. Ahmed TA, Ahmed SM, Elkhenany H, El-Desouky MA, Magdeldin S, Osama A, et al. The cross talk between type II diabetic microenvironment and the regenerative capacities of human adipose tissue-derived pericytes: A promising cell therapy. Stem Cell Res Ther. 2024; 15: 1-18.
13. Banerjee S, Nau S, Hochwald SN, Xie H, Zhang J. Anticancer properties and mechanisms of botanical derivatives. Phytomedicine Plus. 2023; 3: 100396.
14. Navarrete A, Katragunta K, Balderas-López JL, Avula B, Khan IA. Chemical profiling and quantification of flavones in several Pseudognaphalium and Gnaphalium species of Mexican gordolobo using UHPLC/PDA/MS. J Pharm Biomed Anal. 2024; 245: 116186.
15. Aryal S, Baniya MK, Danekhu K, Kunwar P, Gurung R, Koirala N. Total phenolic content, flavonoid content and antioxidant potential of wild vegetables from western Nepal. Plants (Basel). 2019; 8: 96.
16. Herdiana Y, Wathoni N, Shamsuddin S, Muchtaridi M. Drug release study of the chitosan-based nanoparticles. Heliyon. 2022; 8: e08674.
17. Kumar DA, Dharmendra S, Jhansee M, Shrikant N, P PS, S VB. Development and characterization of chitosan nanoparticles. Int Res J Pharm. 2011; 2: 145-151.
18. Li J, Cai C, Li J, Li J, Li J, Sun T, et al. Chitosan-based nanomaterials for drug delivery. Molecules. 2018; 23: 2661.
19. Kendeson CA. Isolation and characterization of flavonoids from Myosotis scorpioides L. (Boraginaceae) and evaluation of antimalarial efficacy of dichloromethane extract of the plant. 2025; 10: 68-79.
20. Kaur P, Arora S, Singh R. Isolation, characterization and biological activities of betulin from Acacia nilotica bark. Sci Rep. 2022; 12: 1-11.
21. Rasul MG. Extraction, isolation and characterization of natural products from medicinal plants. Int J Basic Sci Appl Comput. 2018; 2: 1-6.
22. Mphahlele MP, Mallé Lando A, Kamdem Kengne MH, Tonga Lembe J, Jiyane P, Fonkui Youmbi T, et al. Isolation and characterization of a novel glycoside from the inner bark of Sclerocarya birrea: Insights into antibiotic and anticancer activity. Nat Prod Res. 2025; 39: 1-12.
23. Rosandy AR, Din LB, Yaacob WA, Yusoff NI, Sahidin I, Latip J, et al. Isolation and characterization of compounds from the stem bark of Uvaria rufa (Annonaceae). Malays J Anal Sci. 2013; 17: 50-58.
24. Purushothaman R, Vishnuram G, Ramanathan T. Isolation and identification of n-hexadecanoic acid from Excoecaria agallocha L. and its antibacterial and antioxidant activity. 2024; 11: 332-342.
25. Ahmad N, Khan MR, Palanisamy S, Mohandoss S. Anticancer drug-loaded chitosan nanoparticles for in vitro release, promoting antibacterial and anticancer activities. Polymers (Basel). 2023; 15: 3925.
26. Deng QY, Zhou CR, Luo BH. Preparation and characterization of chitosan nanoparticles containing lysozyme. Pharm Biol. 2006; 44: 336-342.
27. Farmoudeh A, Shokoohi A, Ebrahimnejad P. Preparation and evaluation of the antibacterial effect of chitosan nanoparticles containing ginger extract tailored by central composite design. Adv Pharm Bull. 2021; 11: 643-650.
28. Jha R, Mayanovic RA. A review of the preparation, characterization, and applications of chitosan nanoparticles in nanomedicine. Nanomaterials (Basel). 2023; 13: 1302.
29. Li S, Zhang H, Chen K, Jin M, Vu SH, Jung S, et al. Application of chitosan/alginate nanoparticle in oral drug delivery systems: Prospects and challenges. Drug Deliv. 2022; 29: 1142-1149.
30. Jafernik K, Ładniak A, Blicharska E, Czarnek K, Ekiert H, Wiącek AE, et al. Chitosan-based nanoparticles as effective drug delivery systems: A review. Molecules. 2023; 28: 1963.
31. Justus CR, Leffler N, Ruiz-Echevarria M, Yang LV. In vitro cell migration and invasion assays. J Vis Exp. 2014; 88: 51046.
32. Foster K, Oyenihi O, Rademan S, Erhabor J, Matsabisa M, Barker J, et al. Selective cytotoxic and anti-metastatic activity in DU-145 prostate cancer cells induced by Annona muricata L. bark extract and phytochemical annonacin. BMC Complement Med Ther. 2020; 20: 1-15.

33. Nelson VK, Sahoo NK, Sahu M, Sudhan HH, Pullaiah CP, Muralikrishna KS. In vitro anticancer activity of Eclipta alba whole plant extract on colon cancer cell HCT-116. BMC Complement Med Ther. 2020; 20: 1-8.

34. Zhao K, Pu S, Sun L, Zhou D. Gentiopicroside-loaded chitosan nanoparticles inhibit TNF-α-induced proliferation and inflammatory response in HaCaT keratinocytes and ameliorate imiquimod-induced dermatitis lesions in mice. Int J Nanomedicine. 2023; 18: 3781-3800.

35. Wang J, He X, Jia Z, Yan A, Xiao K, Liu S, et al. Shenqi Fuzheng injection restores the sensitivity to gefitinib in non-small cell lung cancer by inhibiting the IL-22/STAT3/AKT pathway. Pharm Biol. 2024; 62: 33-41.

36. Onyancha JM, Gikonyo NK, Wachira SW, Mwitari PG, Gicheru MM. Anticancer activities and safety evaluation of selected Kenyan plant extracts against breast cancer cell lines. J Pharmacogn Phyther. 2018; 10: 21–26.

37. Kirsh SM, Pascetta SA, Uniacke J. Spheroids as a 3D model of the hypoxic tumor microenvironment. In: Ursini-Siegel J, editor. The Tumor Microenvironment: Methods and Protocols. New York (NY): Springer US; 2023. p. 273–285.

38. Li L, He L, Wu Y, Zhang Y. Carvacrol affects breast cancer cells through TRPM7 mediated cell cycle regulation. Life Sci. 2021; 266.

39. Zhang X, Xu R, Feng W, Xu J, Liang Y, Mu J. Autophagy-related genes contribute to malignant progression and have a clinical prognostic impact in colon adenocarcinoma. Exp Ther Med. 2021; 22: 1–11.

40. Vellky JE, Ricke WA. Development and prevalence of castration-resistant prostate cancer subtypes. Neoplasia. 2020; 22: 566–575.

41. Ren L, Ruan X, Dong H, Cheng Y, Shon K, Chang C, et al. The bitter flavor of Banxia Xiexin decoction activates TAS2R38 to ameliorate low-grade inflammation in the duodenum of mice with functional dyspepsia. J Ethnopharmacol. 2025; 341: 119309.

42. Song X, Shao Z, Han M, Liang H. A novel mouse model of orthotopic extrahepatic cholangiocarcinoma confirmed with molecular imaging. Transl Cancer Res. 2019; 8: 583–591.

43. Ma W, Zhan Y, Zhang Y, Mao C, Xie X, Lin Y. The biological applications of DNA nanomaterials: current challenges and future directions. Signal Transduct Target Ther. 2021; 6.

44. Kroon P, Berry PA, Stower MJ, Rodrigues G, Mann VM, Simms M, et al. JAK-STAT blockade inhibits tumor initiation and clonogenic recovery of prostate cancer stem-like cells. Cancer Res. 2013; 73: 5288–5298.

45. Jiang L, Wang W, He Q, Wu Y, Lu Z, Sun J, et al. Oleic acid induces apoptosis and autophagy in the treatment of tongue squamous cell carcinomas. Sci Rep. 2017; 7: 1–11.

46. Jia L, Jin H, Zhou J, Chen L, Lu Y, Ming Y, et al. A potential anti-tumor herbal medicine, Corilagin, inhibits ovarian cancer cell growth through blocking the TGF-β signaling pathways. BMC Complement Altern Med. 2013; 13: 33.

47. Zhao H, Wu L, Yan G, Chen Y, Zhou M, Wu Y, et al. Inflammation and tumor progression: signaling pathways and targeted intervention. Signal Transduct Target Ther. 2021; 6.

48. Younes I, Rinaudo M. Chitin and chitosan preparation from marine sources: Structure, properties and applications. Mar Drugs. 2015; 13: 1133–1174.

49. Journal B, Sciences A. Chitosan nanoparticles loaded with Mimusops elengi L. stembark extract ameliorate erectile dysfunction disorder by inhibition of pro-erectile dysfunction enzymes. 2024; 17: 69–85.

50. Tawfik E, Ahmed MF. Chitosan nanoparticles as a new technique in gene transformation into different plants tissues. Nat Resour Hum Heal. 2022; 2: 215–221.

51. Sayed AA, Abdel Moteleb MM, El Shafee E, Hanna DH. Oral drug delivery vehicle for insulin and curcumin based on egg albumin-dextran conjugate: In vitro and in vivo studies. J Drug Deliv Sci Technol. 2024; 100: 106052.

52. Ahlidja W, Amegayibor EF, Addae L, Abor EK, Korsah HM, Opoku-Kwabi D, et al. Pharmacological and phytochemical properties of a promising African medicinal plant, Sterculia setigera Delile: A systematic review. Sci African. 2024; 24: e02142.

53. Mekonnen AN, Asrade Atnafie S, Wahab Atta MA. Evaluation of antiulcer activity of 80% methanol extract and solvent fractions of the root of Croton macrostachyus Hochst. ex Del. (Euphorbiaceae) in rodents. Evid Based Complement Alternat Med. 2020; 2020.

54. Sahu G, Patra SA, Lima S, Das S, Görls H, Plass W, et al. Ruthenium(II)-dithiocarbazates as anticancer agents: Synthesis, solution behavior, and mitochondria-targeted apoptotic cell death. Chem Eur J. 2023; 29.

55. Moriasi G, Ngugi M, Mwitari P, Omwenga G. Antioxidant, antiprostate cancer potential, and phytochemical composition of the ethyl acetate stem bark extract of Boascia coriacea (Pax.). PLoS One. 2024; 19: 1–19.

56. Badal S, Delgoda R. Pharmacognosy. London: Academic Press; 2017.

57. Moniruzzaman M, Mannan MA, Hossen Khan MF, Abir AB, Afroze M. The leaves of Crataeva nurvala Buch-Ham. modulate locomotor and anxiety behaviors possibly through GABAergic system. BMC Complement Altern Med. 2018; 18: 1–12.